OPEN ACCESS
IOP Publishing
Plasma Sources Science and Technology
Plasma Sources Sci. Technol. **26** (2017) 025006 (10pp)
doi:10.1088/1361-6595/26/2/025006

On the E-H transition in inductively coupled radio frequency oxygen plasmas: I. Density and temperature of electrons, ground state and singlet metastable molecular oxygen

Th Wegner[1], **C Küllig and J Meichsner**

Institute of Physics, University of Greifswald, Felix-Hausdorff-Str. 6, 17489 Greifswald, Germany

E-mail: physics@thwegner.com and meichsner@physik.uni-greifswald.de

Received 29 July 2016, revised 9 October 2016
Accepted for publication 18 November 2016
Published 19 January 2017

Abstract

In this series of two papers, the E-H transition in a planar inductively coupled radio frequency discharge (13.56 MHz) in pure oxygen is studied using comprehensive plasma diagnostic methods. The electron density serves as the main plasma parameter to distinguish between the operation modes. The (effective) electron temperature, which is calculated from the electron energy distribution function and the difference between the floating and plasma potential, halves during the E-H transition. Furthermore, the pressure dependency of the RF sheath extension in the E-mode implies a collisional RF sheath for the considered total gas pressures. The gas temperature increases with the electron density during the E-H transition and doubles in the H-mode compared to the E-mode, whereas the molecular ground state density halves at the given total gas pressure. Moreover, the singlet molecular metastable density reaches 2% in the E-mode and 4% in the H-mode of the molecular ground state density. These measured plasma parameters can be used as input parameters for global rate equation calculations to analyze several elementary processes. Here, the ionization rate for the molecular oxygen ions is exemplarily determined and reveals, together with the optical excitation rate patterns, a change in electronegativity during the mode transition.

Keywords: inductively coupled plasma, oxygen, mode transition, microwave interferometry, Langmuir probe, optical emission and absorption spectroscopy

(Some figures may appear in colour only in the online journal)

1. Introduction

Inductively coupled plasmas (ICPs) driven at radio frequency (RF) can operate in different modes. They have unique properties and are attracting increasing interest because of their importance for plasma processing applications [1]. In particular, ICPs are used for the sterilization and decontamination of sensitive surfaces [2–5], plasma etching [6–14], diamond [15, 16] and vapor [17] deposition, particle generation [18, 19] as well as the growth of carbon nanotubes [20]. Additionally, ICPs are used in the atomic clocks of the global positioning system (GPS) [21] and for thrusters in electric propulsion [22]. Furthermore, ICPs have more recently been used in plasma medicine, e.g. the treatment of biomolecules [23–25]. The independent control of the energetic ion flux to the surface by biasing the substrate with an additional RF voltage [26, 27] extends the application of ICPs for material modification. In particular, ICPs containing oxygen as a process gas are often used for plasma surface treatments [9–12,

[1] Present address: Max-Planck-Institute for Plasma Physics, Wendelsteinstr. 1, 17491 Greifswald, Germany

14, 23, 24, 28]. Apart from the wide application field, fundamental research of this discharge, and in particular the study of the different operation modes, is still an ambitious task.

For low RF power, the ICP operates in E-mode with a low plasma density and high sheath voltage. Increasing the RF power, mode transition takes place and the discharge operates in the H-mode with a high plasma density and low sheath voltage. For low total gas pressures, this mode transition is continuous and a hybrid mode (E/H) can be observed [29]. The different modes affect the plasma parameters and hence the field of application. Investigation of the mode transition is an important issue for understanding the physics behind this feature. The E-H transition has been investigated in the literature regarding potentials and currents [30–35], the electron density [31, 33–42], the electron energy distribution function (EEDF) [38, 39, 41, 43, 44] and the heating mechanisms [27, 29, 40, 45–49]. Nevertheless, the mode transition of a pure oxygen ICP has only sparsely been studied.

Fuller *et al* [50] investigated a transformer-coupled oxygen plasma by optical emission spectroscopy and Langmuir probe diagnostics at a total gas pressure of 1.3 Pa. They determined the atomic oxygen density in the ground state and the electron temperature for the E- and H-mode. In the work, a decrease in the electron temperature during the E-H transition and a slight increase in the H-mode is reported. Furthermore, they show that the atomic oxygen density in the ground state increases by about two orders of magnitude during the E-H transition. Nevertheless, this density is one order of magnitude lower compared to other publications [39, 51, 52]. Moreover, they used rare gases in the admixture, such as He, Ar, Ne, Kr and Xe, which strongly influence the discharge [34]. Corr *et al* [39] studied the discharge kinetics of a pure oxygen ICP for a total gas pressure ranging from 0.5–6.7 Pa, and compared their experimental results with a global model. Moreover, the authors measured the electron and negative atomic oxygen ion density and showed that electronegativity in the E-mode is higher compared to the H-mode. Additionally, they determined the atomic oxygen density in the ground state and reported an increase from $10^{18}\,\mathrm{m}^{-3}$ in the E-mode to about $10^{20}\,\mathrm{m}^{-3}$ in the H-mode. This is combined with an increase in the dissociation degree of two orders of magnitude during the E-H transition. Corr *et al* also reported on the negative ion loss processes, which are dominated by detachment from the singlet molecular metastable state and atomic ground state at a total gas pressure above 1 Pa. Nevertheless, they did not observe a hybrid mode, which could be due to the relatively poor RF power resolution during the mode transition.

This is the first paper in a series of two, which presents and discusses the experimental results combined with the global rate equation calculation on the E-H transition in a pure oxygen discharge. We used comprehensive plasma diagnostics to study the plasma parameters during the mode transition with a high RF power resolution. In this contribution, we determined the electron density, the floating and plasma potential, the electron and gas temperature as well as the density of the molecular ground state and the singlet molecular metastable state. These findings can be used as input parameters for global rate equation calculations, e.g. the electron impact ionization rate, using the measured densities and rate coefficients from the literature. The second paper in this series focuses on the determination of the negative atomic ion density and the electronegativity, which strongly influence the properties of the plasma [53]. The negative atomic ion density was determined by two experimental methods (laser photodetachment and microwave interferometry) and a global rate equation calculation.

The paper first explains the experimental setup and the applied diagnostics. Secondly, the electron density behavior is discussed for different oxygen pressures; together with the measured coil voltage, this enables a clear distinction between the different operation modes to be made. Thirdly, measurement of the floating and plasma potential allows an estimation for the electron temperature and a comparison with the electron temperature calculated from the EEDF. Deviations found in the E-mode may be due to a change in the electronegativity. Fourthly, spectroscopic measurement of the gas temperature enables the deconvolution of the line-integrated molecular ground state and the singlet molecular metastable state density, which strongly influence the discharge. The ionization rate is determined in the last part of this contribution, also revealing decreasing electronegativity during the E-H transition.

2. Experimental setup and diagnostics

2.1. Vacuum chamber and discharge arrangement

The experiment is composed of the vacuum chamber, the discharge arrangement and the plasma diagnostics, see figure 1. The cylindrical vacuum vessel (400 mm in diameter) and the planar discharge configuration have previously been described in Wegner *et al* [34]. For low-pressure plasma processing, the grounded vacuum chamber was equipped with pumps and control units. A turbomolecular pump set the base pressure at less than 10^{-5} Pa. During the plasma process, a rotary vane pump adjusted the total gas pressure p between 1 and 35 Pa. Oxygen was used as the processing gas at a constant gas flow rate of 5 sccm. The inductively coupled discharge configuration consisted of a planar double spiral antenna with 2.75 windings, which was installed in a quartz cylinder acting as a dielectric barrier. This discharge configuration was immersed in the vacuum vessel from above. The plasma was axially generated between the bottom of the quartz cylinder (120 mm in diameter) at $a = 0$ and the top of a grounded stainless steel electrode (100 mm in diameter) at $a = 50$ mm. The RF power was transferred into the central connection ($r = 0$) of the coil using a 13.56 MHz power generator, which was coupled to a tuning matching network. The two opposite ends of the coil were at ground potential. The input RF power was varied between 1 and 600 W yielding a (peak-to-peak) coil voltage between 1 and 9 kV and a current between 10 and 50 A, respectively. For low RF power values, and in the region of the E-H transition, the RF power resolution was 1 W and the matching network was fixed to exclude its influence on the discharge parameters. Hence, the reflected RF power was smaller than 5% of the input RF power. For the electron density measurement by means of microwave interferometry, the discharge was pulsed

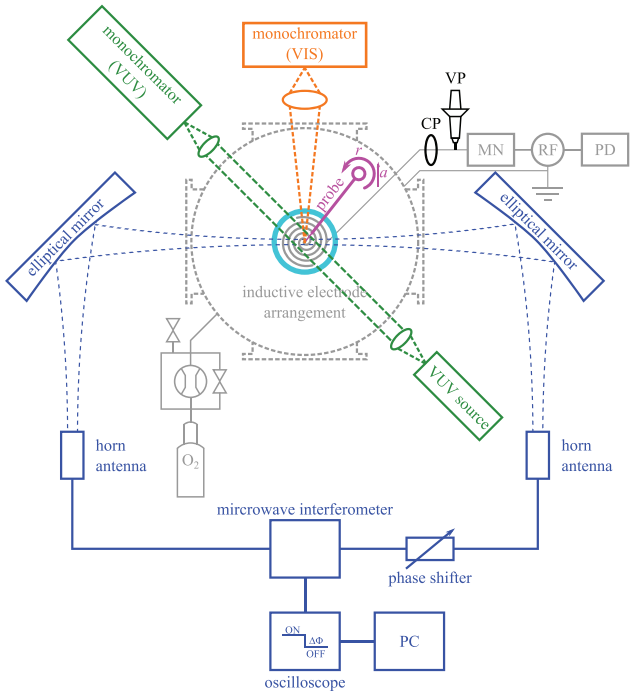

Figure 1. A schematic top view of the discharge vessel with the gas supply, matching network (MN), power supply (RF) and pulse delay generator (PD). The diagnostics used are the current (CP) and voltage probes (VP), the axially (a) and radially (r) movable Langmuir probe, the 160 GHz microwave interferometer, and two monochromators for the optical emission (VIS) and absorption (VUV) spectroscopy, respectively.

with a frequency of 10 Hz and a duty cycle of 50%, allowing an accurate reference signal in the plasma-off phase.

2.2. Plasma diagnostics

A cylindrical Langmuir probe was installed to diagnose the whole plasma volume and to measure the plasma parameters, e.g. the positive ion saturation current and effective electron temperature. The probe system and an analysis of the probe's characteristics has been explained by Küllig *et al* [54]. The whole probe system (150 mm in length) consists of a cylindrical platinum tip (250 μm in diameter and 8 mm in length) and ceramic insulation. It is both axially (a) and radially (r) movable. A passive RF compensation electrode and additional RF filters reduce the disturbing influence of the RF voltage. Measurements of the space-resolved positive ion saturation current were done by biasing the probe 30 V negative to the floating potential, yielding an applicable degree of saturation. In particular, a change in the voltage of ± 5 V at this probe bias led to an ion current variation in the E-mode of less than 5% / V and in the H-mode of less than 2% / V, respectively. The local plasma parameters were measured in the center of the discharge ($r = 0$) at the optical axis of the microwave beam ($a = 30$ mm).

A non-invasive 160 GHz Gaussian beam microwave interferometer reveals information about the line-integrated electron density at $a = 30$ mm and is described in detail by Dittmann *et al* [55]. The measurement of the phase shift $\Delta\Phi$ between the plasma-on and -off phases provides the line-integrated electron density $\tilde{n}_e$, without any model assumptions, using

$$\Delta\Phi = \frac{\pi}{n_C\ \lambda_{MWI}} \int n_e(r)\ \mathrm{d}r = \frac{\pi}{n_C\ \lambda_{MWI}}\ \tilde{n}_e, \qquad (1)$$

where λ_{MWI}, n_C and $n_e(r)$ are the microwave wavelength, the critical electron density and the radial distribution of the electron density along the microwave optical axis, respectively. The resolution of the line-integrated electron density is about 5.3×10^{13} m^{-2}, and the electronics, such as the filters and video amplifier, limit the temporal resolution to about 200 ns.

Analysis of the plasma-induced optical emission of an oxygen discharge in the visible (VIS) wavelength range between 763–774 nm (atmospheric A-bands) provides the rotational temperature of the excited state $O_2(b^1\Sigma_g^+, \nu = 0)$. The emission intensity was measured at the position of the microwave optical axis ($a = 30$ mm) via lenses (focused on the discharge axis $r = 0$) and quartz fiber to the entrance slit of a Czerny–Turner monochromator (Spex 750 M). The applied charged coupled device (CCD) camera allows the analysis of a spectral range over about 30 nm with a spectral resolution of 27 pm. The excited state $O_2(b^1\Sigma_g^+, \nu = 0)$ is highly populated due to efficient creation by collisions and low quenching [56]. The rotational temperature was determined by analyzing the emission intensity of long-living states in the P-branch (763–774 nm) of the forbidden atmospheric A-bands $O_2(b^1\Sigma_g^+, \nu = 0) \longrightarrow O_2(X^3\Sigma_g^-, \nu = 0)$. In particular, the intensity I of the transition from the upper level J' to the lower level J'' is given by

$$I_{J''}^{J'} = C S_{J''}^{J'} \exp\left(\frac{-F_{J'} hc}{k_B T_{rot}}\right), \qquad (2)$$

where C is a constant of proportionality, $S_{J''}^{J'}$ is the Hönl–London factor, $F_{J'}hc$ is the rotational energy where h is the Planck constant, c is the speed of light in a vacuum, k_B is the Boltzmann constant and T_{rot} is the rotational temperature [56]. From a Boltzmann plot with $\ln(I_{J''}^{J'} / S_{J''}^{J'})$ over $F_{J'}$ one can determine the rotational temperature.

Furthermore, vacuum ultraviolet (VUV) absorption spectroscopy enables the determination of the line-integrated molecular ground state $O_2(X^3\Sigma_g^-)$ and the singlet molecular metastable $O_2(a^1\Delta_g)$ density, respectively. A deuterium lamp is installed in the opposite direction of a VUV-monochromator (Acton Research Corp. VM-521-SG) and emits in the appropriate VUV wavelength range. A plano-convex lens behind the lamp enlarges and approximately parallelizes the VUV radiation, which is guided through the center of the discharge at the optical axis position of the microwave beam ($r = 0$, $a = 30$ mm). Another convex lens focuses the transmitted VUV radiation on the entrance slit of the monochromator. The width of the slit defines the spectral resolution to be about 50 pm. The focused light is diffracted by a movable grating which reflects the spectral dispersed light towards a photomultiplier. The lenses and the windows are made of MgF_2

(cutoff wavelength 115 nm) because of its high transmittance in the appropriate VUV wavelength range. The deuterium lamp, the whole path of the emitted light and the monochromator are evacuated to avoid VUV absorption from ambient air. The molecular ground state and the singlet molecular metastable state absorb in the wavelength range between 120–140 nm [57]. A wavelength of $\lambda_l = 134$ nm was used for the determination of the molecular ground state density because the absorption cross section of the molecular ground state is relatively high ($\sigma_X(\lambda_l) = 24 \times 10^{-23}$ m^2), whereas the absorption cross section of the singlet molecular metastable state is low ($\sigma_a(\lambda_l) = 4.7 \times 10^{-23}$ m^2) [57]. Furthermore, the density of the singlet molecular metastable state is low compared to the molecular ground state, and can be neglected during the measurement at the wavelength λ_l. Hence, the line-integrated molecular ground state density $\tilde{n}_X$ is deduced from the intensity ratio between the intensity I (with plasma) and I_0 (vacuum) and using the Lambert–Beer law

$$\tilde{n}_X = \ln\left(\frac{I_0}{I(\lambda_l)}\right)\frac{1}{\sigma_X(\lambda_l)}. \quad (3)$$

The absorption cross section for the singlet molecular metastable state has a maximum at $\lambda_2 = 128.5$ nm and amounts to $\sigma_a(\lambda_2) = 165 \times 10^{-23}$ m^2, whereas the absorption cross section of the molecular ground state is $\sigma_X(\lambda_2) = 4.04 \times 10^{-23}$ m^2 [57]. Due to its high density, the absorption by the molecular ground state density has to be taken into account for the determination of the singlet molecular metastable state density with

$$\tilde{n}_a = \frac{\ln\left(\frac{I_0}{I(\lambda_2)}\right) - \sigma_X(\lambda_2)\tilde{n}_X}{\sigma_a(\lambda_2)}. \quad (4)$$

3. Results and discussion

The different operation modes were determined by observing the heating mechanism with phase- and space-resolved optical emission spectroscopy [29]. The transition of the heating mechanisms leads to a change in the process and plasma parameters. Hence, the operation modes can be determined by comparison of the changing heating mechanisms, coil voltage and electron density.

The line-integrated electron density was converted into absolute values taking into account the measured positive ion saturation current profiles along the optical axis of the microwave beam ($a = 30$ mm). The current profiles change in shape during the E-H transition, which affects the effective microwave path length. In particular, the effective microwave path length in the H-mode is about 20% larger compared to the area in the E-mode. Therefore, the line-integrated electron density in the E-mode and in the H-mode were converted using an effective path length of 0.14 and 0.17 m, respectively. Hence, the electron density resolution is about 3×10^{14} m^{-3}. Additionally, the local electron density was determined from the Langmuir probe measurements, and it is lower than the absolute electron density calculated by the microwave interferometry. For example, the electron density determined by

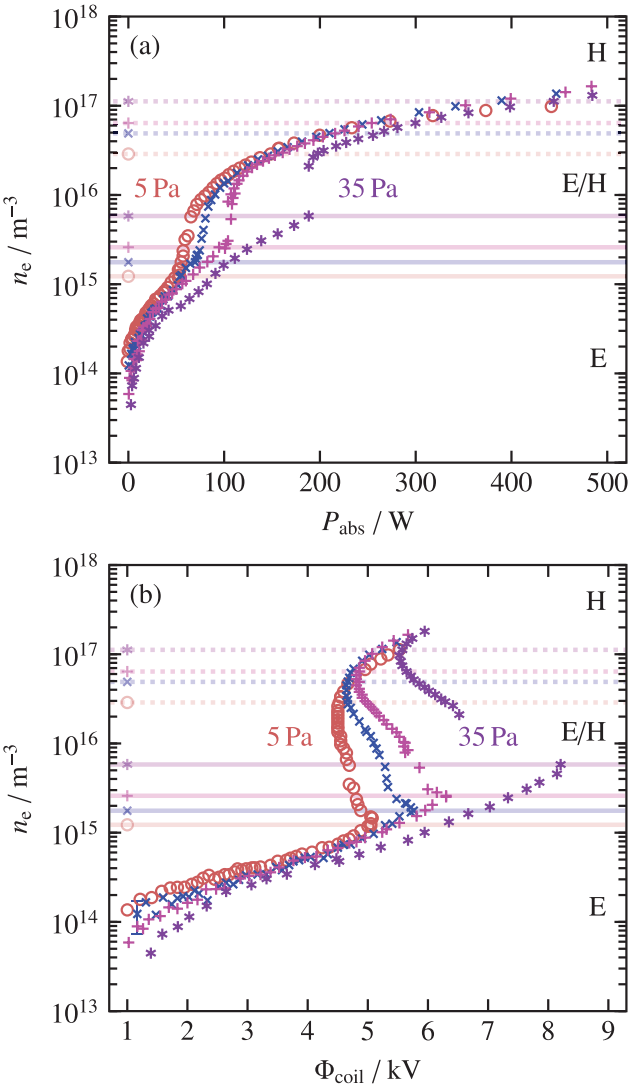

Figure 2. The electron density n_e over the absorbed RF power P_{abs} (a) and the coil voltage Φ_{coil} (b) for different total gas pressures (5 Pa (∘), 10 Pa (×), 15 Pa (+) and 35 Pa (∗)) for the E-mode (E), the hybrid mode (E/H) and for the H-mode (H). The semi-transparent lines with the associated symbols indicate the electron density at which the E-E/H (solid) and the E/H-H (dotted) transition take place.

the microwave interferometry is larger by a factor of 2 in the E-mode, by a factor of 5 in the E/H-mode and by a factor of 4 in the H-mode compared to the electron density in the Langmuir probe measurements. This is well known, and the deviation is comparable to that reported in the literature [54]. In the following, the absolute electron density calculated by the microwave interferometry is considered because of its non-invasiveness, and it is analyzed without using any model assumptions. The electron density is shown in figure 2 over the absorbed RF power (a) and the (peak-to-peak) coil voltage (b). The absorbed RF power was determined by measuring the coil voltage and current involved in the coil resistance [34]. In the E-mode (E), at low RF power the electron density is about 10^{14} m^{-3} for a total gas pressure ranging from 5–35 Pa. Increasing the RF power causes the electron density and the coil voltage to increase weakly. The discharge transits from

the E-mode into the hybrid (E/H) [29] mode at a critical electron density (solid horizontal lines in figure 2), which strongly depends on the total gas pressure (5 Pa: 1×10^{15} m^{-3}, 35 Pa: 6×10^{15} m^{-3}). The transition itself is continuous for a total gas pressure below 30 Pa and step-like above 30 Pa. The electron density is raised by more than one order of magnitude (5 Pa: $\Delta n_e = 2 \times 10^{16}$ m^{-3}, 35 Pa: $\Delta n_e = 1 \times 10^{17}$ m^{-3}) in the hybrid mode, increasing the RF power because of the more efficient inductive heating, which additionally occurs in the hybrid mode [29]. The coil voltage decreases (5 Pa: $\Delta\Phi_{coil} = 0.5$ kV, 35 Pa: $\Delta\Phi_{coil} = 2.5$ kV) due to a changing phase shift between the voltage and current [34]. The discharge operates in the pure H-mode (H) beginning at a higher critical electron density (dotted horizontal lines in figure 2). The coil voltage starts to increase when the discharge is operated mainly in the H-mode; this can be achieved by further increasing the RF power. The electron density in the H-mode is about 10^{17} m^{-3}.

In the following, the measured plasma parameters, which can be used as input parameters for, e.g. global rate equation calculations, are presented over the electron density. This means that the E-mode is on the left-hand side of the solid vertical lines which indicate the E-E/H transition. The hybrid mode can be found between the solid and dotted lines, whereas the H-mode is on the right-hand side of the dotted lines, indicating the E/H-H transition. Furthermore, the following results are presented for a maximum 15 Pa, because use of the invasive Langmuir probe at a higher total gas pressure induces the E-H transition.

The floating and the plasma potential are given in figures 3(a) and (b), respectively. Both parameters increase when the electron density in the E-mode is raised; however, the floating potential reaches a maximum at the E-E/H transition and decreases for higher electron densities. This behavior is consistent with the results reported in the literature [32], and the plasma potential behaves quite similarly. Nevertheless, the maximum value of the plasma potential can be observed just before the E-E/H transition. The floating Φ_{fl} and the plasma Φ_{pl} potential can be used to estimate the effective electron temperature T_e [58]. There is assumed to be a collisionless sheath in front of the floating surface, as well as cold ions, Maxwellian electrons and an electropositive plasma. Hence, the effective electron temperature can be determined using

$$\Phi_{pl} - \Phi_{fl} = \frac{1}{2}\frac{k_B T_e}{e}\left[1 + \ln\left(\frac{m_+}{2\pi m_e}\right)\right], \qquad (5)$$

where k_B, e, m_+ and m_e are the Boltzmann constant, the elementary charge, the mass of the positive ions and the electron mass, respectively [58]. The measured effective electron temperature from the evaluation of the probe characteristic is shown in figure 4(a). The EEDF in the E-mode is bi-Maxwellian while the EEDF in the H-mode is nearly Maxwellian, as is also known from the literature [44, 59, 60]. Hence, the given electron temperature in the E-mode should be recognized as an average electron energy corresponding to an effective electron temperature. The effective electron temperature is high compared to the H-mode and nearly constant at about 6.5 eV. Before the E-E/H transition, the effective electron temperature will already have decreased strongly, usually reaching its minimum value at an E-E/H transition of about 2–3 eV, depending on the total gas pressure. This is comparable to other works [50, 52].

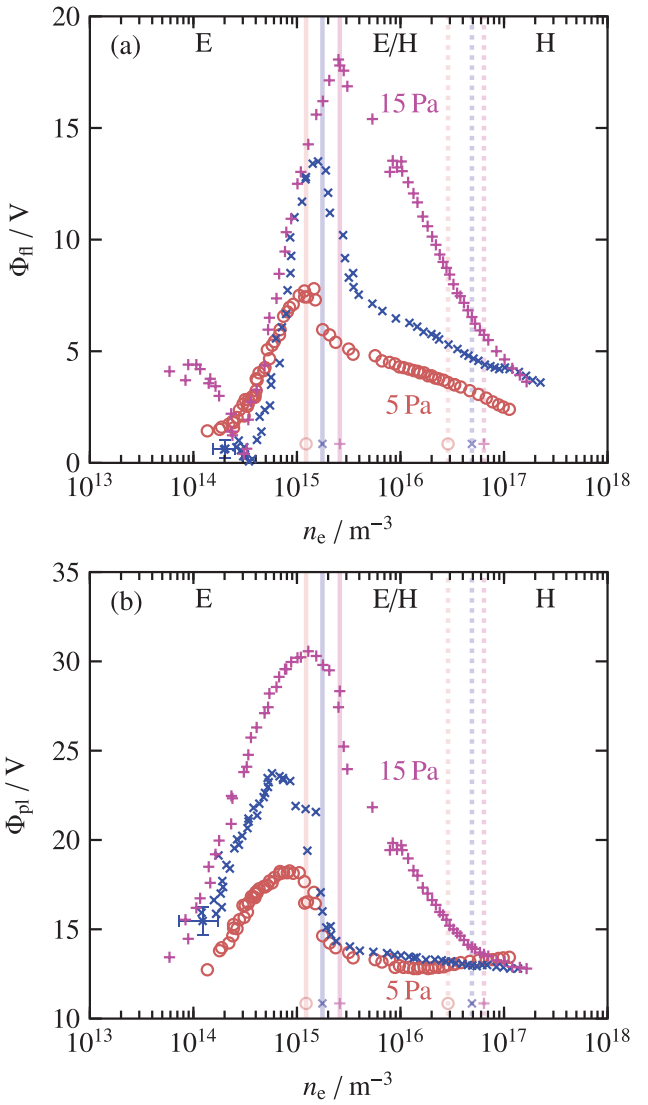

Figure 3. The floating Φ_{fl} (a) and plasma potential Φ_{pl} (b) over the electron density n_e for different total gas pressures (5 Pa (∘), 10 Pa (×) and 15 Pa (+)) for the E-mode (E), the hybrid mode (E/H) and for the H-mode (H). The semi-transparent lines with the associated symbols indicate the electron density at which the E-E/H (solid) and the E/H-H (dotted) transition take place.

The increase in electron density leads to an increase in the electron–electron collision frequency ν_{ee}, which is proportional to the electron density and inversely proportional to the electron temperature, $\nu_{ee} \propto n_e/T_e^{3/2}$ [44, 61, 62]. Hence, the elastic electron–electron interaction becomes more important. As a result, the two electron energy populations in the E-mode thermalize, and the EEDF evolves from a bi-Maxwellian to a Maxwellian distribution in the E/H and H-mode. Furthermore, the effective electron temperature decreases with an increase in total gas pressure. At these total gas pressures one can assume a collision-dominated regime; hence, the electron-heavy

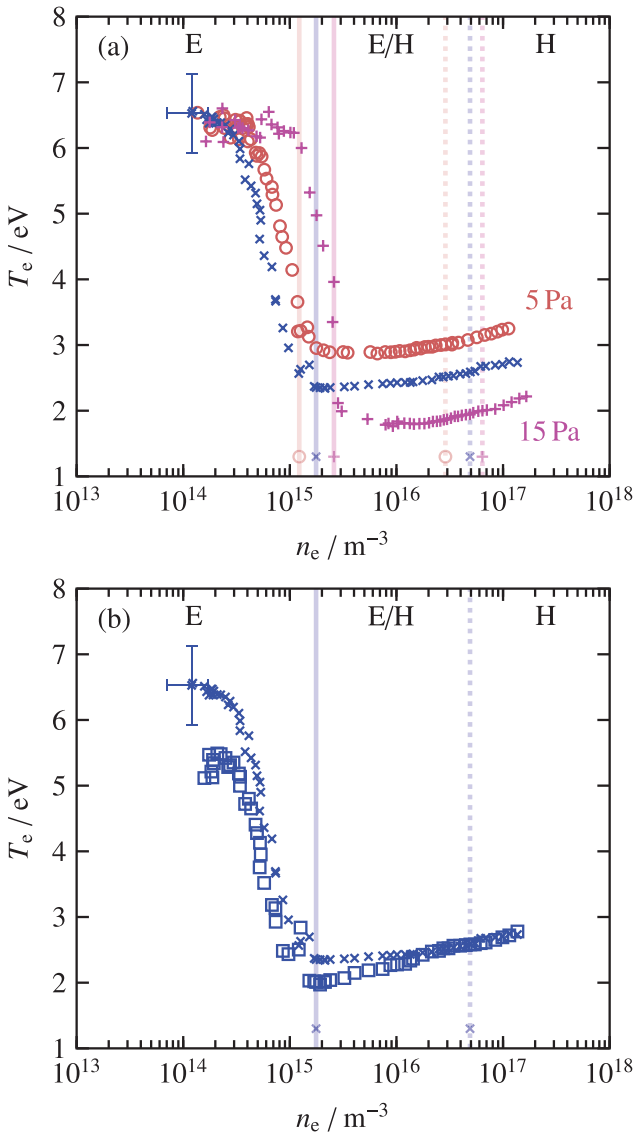

Figure 4. The effective electron temperature T_e calculated from the EEDF (a) for different total gas pressures (5 Pa (∘), 10 Pa (×), 15 Pa (+)) and (b) a comparison between the effective electron temperature (×) calculated from the EEDF and the electron temperature (□) calculated from the potential difference (equation (5)) for 10 Pa over the electron density n_e for the E-mode (E), the hybrid mode (E/H) and for the H-mode (H). The semi-transparent lines with the associated symbols indicate the electron density at which the E-E/H (solid) and the E/H-H (dotted) transition take place.

particle collision rate increases when the pressure is raised, which explains the pressure dependency of the electron temperature mentioned above [39]. This behavior has previously been reported for ICPs [39, 52, 59, 63] and CCPs [61]. After the E/H-H transition, the effective electron temperature slightly increases. A comparison between the electron temperature calculated from the EEDF and estimated from the potential difference is shown in figure 4(b), and both methods reveal comparable results. The greatest deviation can be found in the E-mode, where the phase-resolved optical emission spectroscopy reveals an excitation rate pattern during the sheath collapse phase, which is connected to the electric field reversal

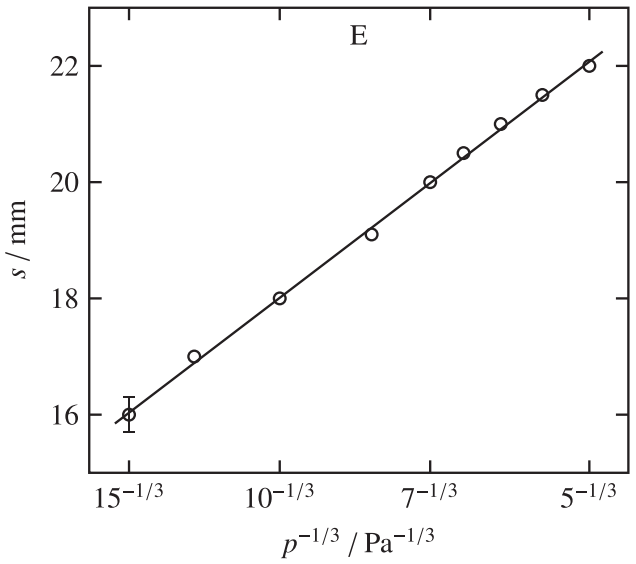

Figure 5. The pressure dependency of the axial distance of the maximum positive ion saturation current s as a measure of the RF sheath extension in the E-mode.

and is an indication for high electronegativity [29]. Hence, the assumption of an electropositive plasma is mostly broken in the E-mode, which might be an explanation for the deviation. Additionally, the high effective electron temperature in the E-mode can be explained regarding the high electronegativity, as high electronegativity leads to a lower electron density compared to an electropositive plasma. Hence, the electrons have to be fast enough to ionize and therefore sustain the plasma. To support the collision-dominated regime at these total gas pressures, one can analyze the pressure dependency of the RF sheath extension. Therefore, the axial profile of the positive ion saturation current were measured for different total gas pressures. These profiles are qualitatively comparable to those which were measured in an argon ICP [35]. With a rising pressure the maximum value of the positive ion saturation current increases and its axial distance shifts to the antenna. This axial distance s can be used as a measure for the RF sheath extension, and is shown in figure 5 for a different total gas pressure. An RF sheath only develops in the E-mode, which is dependent on the pressure. The RF sheath extension reveals a $s \propto p^{-1/3}$ pressure dependency, which is also known from the ICP [35] and CCP [54]. Assuming a constant mean RF sheath voltage, this dependency can be an indication of a collision-dominated RF sheath [64].

Another important parameter is the gas temperature. Analysis of the optical emission from a rotationally resolved molecule band enables the determination of the rotational temperature, the latter of which is comparable to the gas temperature [56]. This is only valid when the energy exchange between the translational and rotational degrees of freedom is faster than the radiative lifetime τ of the excited state. A criterion to estimate this condition is given by [65]

$$p\tau \geqslant 10^{-4}\ \text{Pa s}. \tag{6}$$

Together with a minimum total gas pressure of 5 Pa and a radiative lifetime of the second singlet molecular metastable state

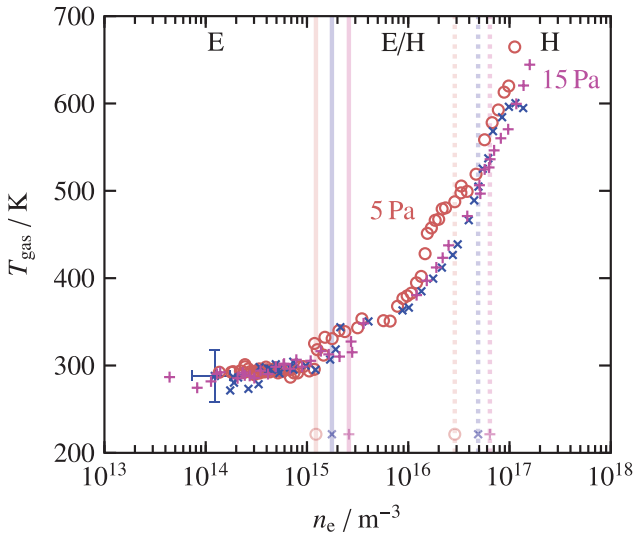

Figure 6. The gas temperature T_{gas} over the electron density n_e for different total gas pressures (5 Pa (∘), 10 Pa (×), 15 Pa (+)) for the E-mode (E), the hybrid mode (E/H) and for the H-mode (H). The semi-transparent lines with the associated symbols indicate the electron density at which the E-E/H (solid) and the E/H-H (dotted) transition take place.

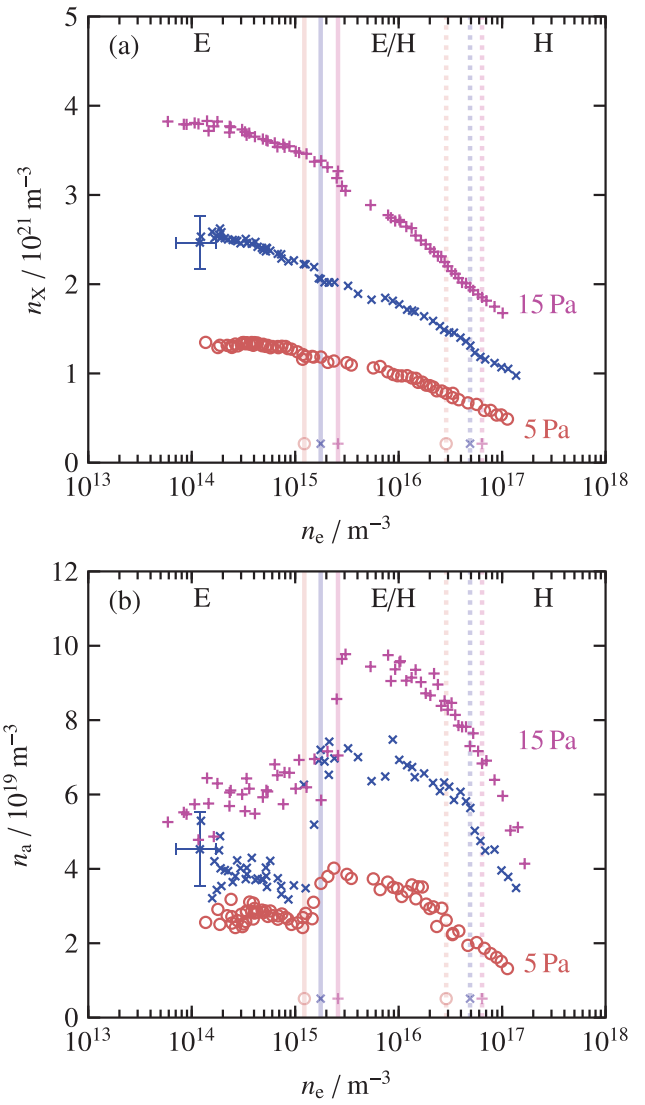

Figure 7. The molecular ground state n_X (a) and the singlet molecular metastable state n_a (b) over the electron density n_e for different total gas pressures (5 Pa (∘), 10 Pa (×) and 15 Pa (+)) for the E-mode (E), the hybrid mode (E/H) and for the H-mode (H). The semi-transparent lines with the associated symbols indicate the electron density at which the E-E/H (solid) and the E/H-H (dotted) transition takes place.

$O_2(b^1\Sigma_g^+)$ of 11.8 s [65], the criterion given above is well fulfilled. Hence, the rotational temperature is assumed to be equal to the gas temperature, as shown in figure 6(a). The gas temperature in the E-mode is nearly constant at room temperature (300 K) and increases at the E-E/H transition up to 600 K in the H-mode. Spectroscopic gas temperature determination by Foucher *et al* [66] provides temperatures which are about 200 K lower; this might be due to the much lower flow rate in our experiment. The main source of gas heating is the dissociation of $O_2(X^3\Sigma_g^-)$. Raising the electron density, the dissociation rate increases, which explains why the gas temperature increases when the electron density is raised. An increasing degree of dissociation with an increase in RF power, and also an increase in electron density, has also been reported by Corr *et al* [39]. This should result in a decreasing molecular ground state density. Furthermore, the gas temperature is not dependent on the considered total gas pressure; hence, the molecular ground state density should increase when the pressure is raised.

To evaluate this, the line-integrated density of the molecular ground state and the singlet molecular metastable state from VUV absorption, respectively, have to be deconvolved into absolute density values. Therefore, the total gas pressure and the partial pressure of each species were considered. The gas temperature and the total gas pressure were used to determine the total particle density in the plasma region. This plasma density was balanced with the density of each species with respect to their temperature. The electrons, the atomic oxygen in the ground state $O(^3P)$, the molecular ground state $O_2(X^3\Sigma_g^-)$ and the singlet molecular metastable $O_2(a^1\Delta_g)$ were considered for this calculation. The density of the atomic oxygen in the ground state was taken from the global model of Corr *et al* [39] for the considered pressures and electron densities, and is comparable to other works [51, 52]. The metastable atom $O(^1D)$, the Herzberg states and the ozone can be neglected due to their low density and temperature [52]. We assumed an equal temperature for the molecular ground state, the singlet molecular metastable state $O_2(a^1\Delta_g)$ and the atomic oxygen in the ground state, respectively. Furthermore, we took into account the same effective optical path length for the molecular ground state and singlet molecular metastable state $O_2(a^1\Delta_g)$. Hence, the molecular ground state and singlet molecular metastable state density were deconvolved, as presented in figures 7(a) and (b), respectively. The behavior of the molecular ground state density regarding the electron density and total gas pressure follows the discussion above for the gas temperature. The molecular ground state density is comparable to the literature [51]. From the ground state density measurements in the plasma (E-mode) and without the plasma one can determine both the dissociation degree and the effective optical

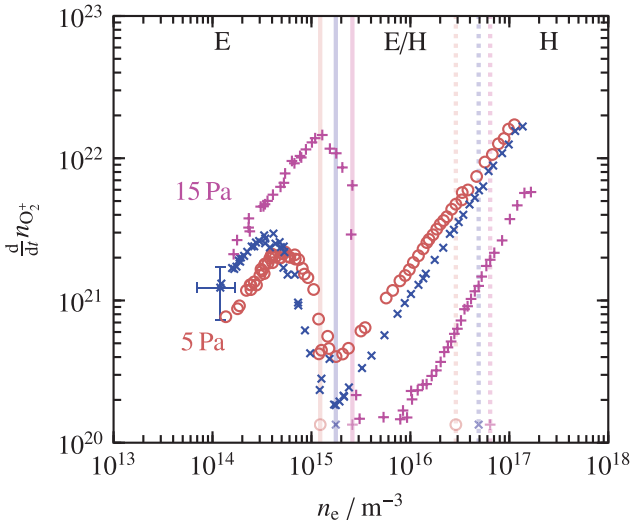

Figure 8. The ionization rate $dn_{O_2^+}/dt$ over the electron density n_e for different total gas pressures (5 Pa (∘), 10 Pa (×) and 15 Pa (+)) for the E-mode (E), the hybrid mode (E/H) and for the H-mode (H). The semi-transparent lines with the associated symbols indicate the electron density at which the E-E/H (solid) and the E/H-H (dotted) transition takes place.

path length, which are comparable to the method mentioned above. The dissociation degree in the E-mode is about 1% and is in agreement with the literature [39]. The singlet molecular metastable density is constant in the E-mode, which is about 2% of the molecular ground state. At the E-E/H transition, the singlet molecular metastable state density suddenly increases by a factor of about 1.5, while the molecular ground state density decreases. This leads to a percentage of about 4% of the molecular ground state density in the E/H and H-mode. In the E/H-mode, the singlet molecular metastable density is comparable to the literature [51] and decreases after the maximum in the E/H-mode. At this point, the atomic density in the ground state becomes comparable to the singlet molecular metastable density, and strongly increases with further rising electron density. Hence, the particle balance has to be fulfilled and the density of the singlet molecular metastable state, as well as the molecular ground state, drop with increasing electron density. This decrease is not yet fully understood and needs to be further investigated. A rate equation calculation for the sources and sinks of the singlet molecular metastable state may give an explanation for this behavior.

As an example, the electron impact ionization rate of the molecular ground state was calculated taking into account the electron density n_e, the electron temperature T_e and the molecular ground state density n_X obtained from measurements and the ionization rate coefficient k_{ion} from the literature [67]. The ionization rate for the main ionization process

$$e + O_2(X^3\Sigma_g^-) \longrightarrow O_2^+ + 2e \tag{7}$$

can thereby be determined with

$$\frac{d}{dt}n_{O_2^+} = k_{ion}(T_e)n_X n_e. \tag{8}$$

The ionization rate is shown in figure 8 over the electron density, and it increases in the E-mode when the electron density is low. Before the E-E/H transition, this ionization rate strongly decreases due to the drop in electron temperature and reaches its minimum at the E-E/H transition. After this transition, the ionization rate increases strongly. Although the ionization rate decreases strongly, the electron density increases; hence, another electron source might have caused this electron release. From the literature, it is known that the electronegativity, which is the ratio between the negative ion density and the electron density, decreases dramatically during the transition from E- to H-mode [39, 51, 60, 68, 69]. This decreasing electronegativity contributes to an increasing electron density, and would explain the behavior of the ionization rate mentioned above. To fully understand this behavior, and to calculate a whole set of rate equations, one needs to know the negative ion density, which is very important for this discharge at the considered total gas pressure [51].

4. Conclusion and summary

This contribution presents and discusses the results of an inductively coupled RF discharge in oxygen. It combines comprehensive plasma diagnostics to study the E-H transition. Three different operation modes were found during the mode transition. With an increase in the RF power, and also the electron density, the discharge transits from the E-mode to the hybrid E/H-mode into the H-mode. The transition points are noticeable in most of the measured plasma parameters.

The floating potential reaches a maximum at the E-E/H transition and the plasma potential reaches its maximum for a lower electron density compared to the critical electron density for the E-E/H transition. The electron temperature calculated from the potential difference is comparable to the electron temperature calculated by the EEDF. The greatest deviation is observable in the E-mode due to the high electronegativity. The electron temperature is high in the E-mode and halves during the E-H transition. The EEDF is bi-Maxwellian in the E-mode and nearly Maxwellian in the H-mode. The pressure dependency of the RF sheath extension reveals a collisional RF sheath. The gas temperature increases by a factor of two during the E-H transition and is not dependent on the considered total gas pressure. However, the molecular ground state density does depend on the total gas pressure and decreases when the electron density is raised due to an increasing degree of dissociation. The singlet molecular metastable density is about 2% and about 4% of the molecular ground state density in the E- and H-mode, respectively. In the H-mode, the singlet molecular metastable density decreases strongly due to the rising atomic density in the ground state.

To summarize, the mode transition fully changes the discharge characteristics and in particular the plasma parameters. Together with these measured plasma parameters and the rate coefficients from the literature one can evaluate the rate equations for elementary processes. Nevertheless, the determination of the negative ion density is an important task and will be focused on in the second part of this series.

Acknowledgments

This work was supported by the Deutsche Forschungsgemeinschaft (DFG) in the framework of the Sonderforschungsbereich Transregio 24 'Fundamentals of Complex Plasmas', project B5.

References

[1] Keller J H 1996 *Plasma Sources Sci. Technol.* **5** 166
[2] Gans T, Osiac M, O'Connell D, Kadetov V A, Czarnetzki U, Schwarz-Selinger T, Halfmann H and Awakowicz P 2005 *Plasma Phys. Control. Fusion* **47** A353
[3] Halfmann H, Bibinov N, Wunderlich J and Awakowicz P 2007 *J. Phys. D: Appl. Phys.* **40** 4145
[4] Stapelmann K, Kylián O, Denis B and Rossi F 2008 *J. Phys. D: Appl. Phys.* **41** 192005
[5] Morent R and Geyter N D 2011 Inactivation of bacteria by non-thermal plasmas *Biomedical Engineering - Frontiers and Challenges* ed Reza Fazel-Rezai (doi:10.5772/18610)
[6] Carter J B, Holland J P, Peltzer E, Richardson B, Bogle E, Nguyen H T, Melaku Y, Gates D and Ben-Dor M 1993 *J. Vac. Sci. Technol.* A **11** 1301
[7] Patrick R, Schoenborn P, Toda H and Bose F 1993 *J. Vac. Sci. Technol.* A **11** 1296
[8] Forgotson N, Khemka V and Hopwood J 1996 *J. Vac. Sci. Technol.* B **14** 732
[9] Im Y H, Park J S, Choi C S, Choi R J, Hahn Y B, Lee S-H and Lee J-K 2001 *J. Vac. Sci. Technol.* A **19** 1315
[10] Shin M H, Park M S, Lee N-E, Kim J, Kim C Y and Ahn J 2006 *J. Vac. Sci. Technol.* A **24** 1373
[11] Carlström C F, van der Heijden R, Karouta F, van der Heijden R W, Salemink H W M and van der Drift E 2006 *J. Vac. Sci. Technol.* B **24** L6
[12] Ono T, Akagi T and Ichiki T 2009 *J. Appl. Phys.* **105** 013314
[13] Ayari-Kanoun A, Jaouad A, Souifi A, Drouin D and Beauvais J 2011 *J. Vac. Sci. Technol.* B **29** 051802
[14] Douglas E A, Stevens J, Fishgrab K, Ford C, Shul R J and Pearton S J 2012 *J. Vac. Sci. Technol.* B **30** 06FF06
[15] Bozeman S P, Tucker D A, Stoner B R, Glass J T and Hooke W M 1995 *Appl. Phys. Lett.* **66** 3579
[16] Teii K and Yoshida T 1999 *J. Appl. Phys.* **85** 1864
[17] Colpo P, Ceccone G, Sauvageot P, Baker M and Rossi F 2000 *J. Vac. Sci. Technol.* A **18** 1096
[18] Bapat A, Perrey C R, Campbell S A, Barry Carter C and Kortshagen U 2003 *J. Appl. Phys.* **94** 1969
[19] Schulze M, von Keudell A and Awakowicz P 2006 *Appl. Phys. Lett.* **88** 141503
[20] Delzeit L, McAninch I, Cruden B A, Hash D, Chen B, Han J and Meyyappan M 2002 *J. Appl. Phys.* **91** 6027
[21] Camparo J and Fathi G 2009 *J. Appl. Phys.* **105** 103302
[22] Neumann H, Tartz M, Scholze F, Chassé T, Kersten H and Leiter H 2007 *Contrib. Plasma Phys.* **47** 487
[23] von Keudell A *et al* 2010 *Plasma Process. Polym.* **7** 327
[24] Kylián O, Denis B, Stapelmann K, Ruiz A, Rauscher H and Rossi F 2011 *Plasma Process. Polym.* **8** 1137
[25] Bartis E A J, Barrett C, Chung T-Y, Ning N, Chu J-W, Graves D B, Seog J and Oehrlein G S 2014 *J. Phys. D: Appl. Phys.* **47** 045202
[26] Keller J H, Forster J C and Barnes M S 1993 *J. Vac. Sci. Technol.* A **11** 2487
[27] Schulze J, Schüngel E and Czarnetzki U 2012 *Appl. Phys. Lett.* **100** 024102
[28] Yoshino K, Matsumoto H, Iwasaki T, Kinoshita S, Noda K and Iwamori S 2013 *Vacuum* **93** 84
[29] Wegner Th, Küllig C and Meichsner J 2015 *Plasma Sources Sci. Technol.* **24** 044001
[30] Kortshagen U, Gibson N D and Lawler J E 1996 *J. Phys. D: Appl. Phys.* **29** 1224
[31] Ostrikov K N, Xu S and Yu M Y 2000 *J. Appl. Phys.* **88** 2268
[32] Kempkes P, Singh S V, Pargmann C and Soltwisch H 2006 *Plasma Sources Sci. Technol.* **15** 378
[33] Singh S V and Pargmann C 2008 *J. Appl. Phys.* **104** 083303
[34] Wegner Th, Küllig C and Meichsner J 2015 *Contrib. Plasma Phys.* **55** 728
[35] Wegner Th, Küllig C and Meichsner J 2016 *Phys. Plasmas* **23** 023503
[36] Amorim J, Maciel H S and Sudano J P 1991 *J. Vac. Sci. Technol.* B **9** 362
[37] Lee M-H and Chung C-W 2006 *Phys. Plasmas* **13** 063510
[38] Lee J-K, Lee H-C and Chung C-W 2011 *Curr. Appl. Phys.* **11** S149
[39] Corr C S, Gomez S and Graham W G 2012 *Plasma Sources Sci. Technol.* **21** 055024
[40] Lishev S, Shivarova A, Tarnev K, Iordanova S, Koleva I, Paunska T and Iordanov D 2013 *J. Phys. D: Appl. Phys.* **46** 165204
[41] Kim J Y, Kim D-H, Kim J H, Jeon S-B, Cho S-W and Chung C-W 2014 *Phys. Plasmas* **21** 113505
[42] Wang J, Du Y-c, Zhang X, Zheng Z, Liu Y, Xu L, Wang P and Cao J-x 2014 *Phys. Plasmas* **21** 073502
[43] Chung C and Chang H-Y 2002 *Appl. Phys. Lett.* **80** 1725
[44] Lee H-C, Lee J-K and Chung C-W 2010 *Phys. Plasmas* **17** 033506
[45] Abdel-Rahman M, Gans T, von der Gathen V S and Döbele H F 2005 *Plasma Sources Sci. Technol.* **14** 51
[46] Kampschulte T, Schulze J, Gans T, Czarnetzki U, Marke S and Wallendorf T 2005 *Surf. Coat. Technol.* **200** 859
[47] Abdel-Rahman M, von der Gathen V S and Gans T 2007 *J. Phys. D: Appl. Phys.* **40** 1678
[48] Zaka-ul Islam M, Niemi K, Gans T and O'Connell D 2011 *Appl. Phys. Lett.* **99** 041501
[49] Wegner Th, Küllig C and Meichsner J 2014 *IEEE Trans. Plasma Sci.* **42** 2830
[50] Fuller N C M, Malyshev M V, Donnelly V M and Herman I P 2000 *Plasma Sources Sci. Technol.* **9** 116
[51] Gudmundsson J T, Kouznetsov I G, Patel K K and Lieberman M A 2001 *J. Phys. D: Appl. Phys.* **34** 1100
[52] Toneli D A, Pessoa R S, Roberto M and Gudmundsson J T 2015 *J. Phys. D: Appl. Phys.* **48** 325202
[53] Wegner Th, Küllig C and Meichsner J 2017 On the E-H transition in inductively coupled radio frequency oxygen discharges: II. Electronegativity and the impact on particle kinetics *Plasma Sources Sci. Technol.* **26** 025007
[54] Küllig C, Wegner Th and Meichsner J 2015 *Plasma Sources Sci. Technol.* **24** 015027
[55] Dittmann K, Küllig C and Meichsner J 2012 *Plasma Sources Sci. Technol.* **21** 024001
[56] Touzeau M, Vialle M, Zellagui A, Gousset G, Lefebvre M and Pealat M 1991 *J. Phys. D: Appl. Phys.* **24** 41
[57] Ogawa S and Ogawa M 1975 *Can. J. Phys.* **53** 1845
[58] Meichsner J, Schmidt M, Schneider R and Wagner H-E 2012 *Nonthermal Plasma Chemistry and Physics* (Boca Raton, FL: CRC Press)
[59] Seo S-H, Chung C-W, Hong J-I and Chang H-Y 2000 *Phys. Rev.* E **62** 7155
[60] Corr C S, Steen P G and Graham W G 2003 *Plasma Sources Sci. Technol.* **12** 265
[61] Godyak V A, Piejak R B and Alexandrovich B M 1992 *Plasma Sources Sci. Technol.* **1** 36
[62] Lieberman A M 2005 *Principles of Plasma Discharges and Materials Processing* (New York: Wiley)
[63] Seo D C, Chung T H, Yoon H J and Kim G H 2001 *J. Appl. Phys.* **89** 4218

[64] Meichsner J, Dittmann K and Küllig C 2012 *Contrib. Plasma Phys.* **52** 561
[65] Zyryanov S M and Lopaev D V 2006 *Plasma Phys. Rep.* **33** 510
[66] Foucher M, Marinov D, Carbone E, Chabert P and Booth J-P 2015 *Plasma Sources Sci. Technol.* **24** 042001
[67] Kimura T, Lichtenberg A J and Lieberman M A 2001 *Plasma Sources Sci. Technol.* **10** 430
[68] Stoffels E, Stoffels W W, Vender D, Kando M, Kroesen G M W and de Hoog F J 1995 *Phys. Rev.* E **51** 2425
[69] Küllig C, Dittmann K and Meichsner J 2010 *Plasma Sources Sci. Technol.* **19** 065011